Asian Journal of Chemistry; Vol. 38, No. 9 (2026), 2371-2386
ASIAN JOURNAL OF CHEMISTRY
https://doi.org/10.14233/ajchem.2026.36470

Computational Exploration of the Structural, Electronic and Nonlinear Optical Properties of Substituted Piperidine Scaffold: A DFT and Molecular Docking Approach

G. BASKAR[1], J.B. VEERAMALINI[2] and J. WINFRED JEBARAJ[3,*]

[1]Department of Chemistry, Sri Venkateswara College of Engineering, Pennalur, Sriperumbudur-602117, India
[2]Department of Chemical Engineering, Vel Tech High Tech Dr. Rangarajan Dr. Sakunthala, Engineering College, Avadi, Chennai-600062, India
[3]Department of Chemistry, St. John's College, Palayamkottai. Tirunelveli-627002, India

*Corresponding author: E-mail: winfred.chem@stjohnscollege.edu.in

Received: 20 May 2026 *Accepted*: 5 August 2026 *Published online*: 5 September 2026 AJC-22465

An investigation into the structural, electronic and reactive properties of a substituted piperidine scaffold were conducted using density functional theory (DFT) at the B3LYP/6-31 G(d) level of theory. Molecular geometry optimization established a stable equilibrium structure. Frontier molecular orbital (FMO) analysis suggested a HOMO-LUMO energy gap of 5.6665 eV, consistent with high kinetic stability. Molecular electrostatic potential (MEP) mapping and Mulliken charge analysis identified the oxygen atoms as the principal nucleophilic centers, while the hydroxyl hydrogen bears a pronounced electrophilic character. Natural bond orbital (NBO) and non-covalent interaction (NCI) analyses quantified pronounced hyperconjugative stabilization and a complex network of hydrogen bonding interactions, particularly across the hydrazone linkage, which exhibited a Mayer bond order of 1.6852. The first-order hyper-polarizability was calculated as 1.044×10^{-30} esu, approximately 2.8-fold higher than that of urea, supporting the potential of the molecule for nonlinear optical (NLO) applications. Thermodynamic parameters exhibited strong temperature dependence, while STM and ALIE surface analyses identified the nitrogen-rich core as an electronically active region. Molecular docking against the 1BP1 protein yielded a binding energy of -6.4 kcal/mol, with hydrogen-bonding interactions involving VAL A:433 and PRO A:430. These computational findings support the relevance of the molecular scaffold for further investigation in medicinal chemistry and optoelectronic applications.

Keywords: Mayer bond, Substituted piperidine, Hydrazine, Molecular docking.

INTRODUCTION

Semicarbazones constitute an important class of nitrogen containing compounds employed as reactive intermediates/ precursors in diverse chemical transformations [1-10]. Their donor-rich frameworks provide versatile coordination sites, enabling their use as effective ligands [11-14]. Piperidin-4-one semicarbazones are particularly relevant owing to the reactivity of the keto-derived carbonyl group. Conventional catalytic reduction of piperidone semicarbazones has been reported [6-8], whereas electrochemical studies of N-substituted piperidin-4-one semicarbazones remain limited [12-15]. The present study focuses on (*E*)-4-(2-(amino(hydroxy)-methyl)hydrazono)-3-ethyl-2,6-diphenylpiperidin-1-ol [6,7], a scaffold incorporating a substituted piperidine ring, hydrazone linkage and hydroxyl containing side chain.

Piperidin-4-one derivatives possess remarkable antifungal [16] and antibacterial activities [8,17,18]. Semicarbazone functionalized piperidines provide multiple nitrogen and oxygen donor sites capable of hydrogen bonding and metal coordination. Related semicarbazones have been investigated for antioxidant, antitubercular and antimicrobial properties [19], while their donor atoms have enabled chemosensing applications toward transition-metal ions such as nickel [20]. These characteristics provide a basis for examining the present scaffold from biological and molecular electronic perspectives.

The investigated molecule combines a 2,6-diphenylpiperidin-1-ol core with a nitrogen-rich hydrazone and amino-(hydroxy)methyl functionality. The phenyl groups contribute structural rigidity, whereas the hydrazone, hydroxyl and amino groups provide multiple donor and acceptor sites. This arrangement permits evaluation of electronic delocalization, charge distribution, hydrogen-bonding interactions and nonlinear optical (NLO) response. These functional groups may further serve as recognition sites during protein binding, linking the electronic and biological characteristics of the molecule.

Density functional theory (DFT) provides an efficient framework for predicting molecular geometries and electronic properties with substantially lower computational cost than conventional wave-function methods [21,22]. DFT calculations were used to optimize the molecular structure and evaluate its electronic properties. Frontier molecular orbitals, molecular electrostatic potential and Mulliken charges were examined to characterize charge distribution and reactive sites. Natural bond orbital (NBO) and non-covalent interaction (NCI) analyses were applied to assess hyperconjugative stabilization and weak interactions, while Mayer bond orders provided insight into the hydrazone bonding character. First-order hyperpolarizability was calculated to assess the NLO response. Thermodynamic parameters, scanning tunneling microscopy (STM) and average local ionization energy (ALIE) surfaces were evaluated to describe molecular behaviour and electronically active regions. Molecular docking with the 1BP1 protein was performed to assess binding affinity and identify key residue interactions. This integrated analysis establishes relationships between molecular structure, electronic stability, NLO response and protein-binding characteristics of the title compound.

COMPUTATIONAL DETAILS

The molecular structure was initially sketched in Chemsketch [23] to obtain the 2D representation, which was subsequently imported into Avogadro [24] for 3D coordinate generation and preliminary geometry optimization. The resulting structure was saved in .pdb format and utilized for high-level electronic structure calculations using the Gaussian 16W [25] software package. The B3LYP/6-31 G(d) bas set [26,27] was utilized to run the jobs in the gaseous phase. To ensure the stability of the optimized geometries, frequency calculations were performed at the same level of theory. The absence of imaginary frequencies confirmed that the structures represented true local minima on the potential energy surface. Visual inspection of the Gaussian 16W output and molecular orbitals was conducted using GaussView 06, while GaussSum 3.0 [28] was employed to monitor the convergence of the energy minimization and confirm full optimization. Detailed wave-function analysis, was carried out using Multiwfn 3.8 [29]. Furthermore, the visualization of electron density and various isosurfaces was rendered using VMD 1.9.7 [30]. For the biological study, molecular docking simulations were executed using PyRx [31], while the Discovery Studio Visualizer [32] was utilized for comprehensive pre-docking preparation and post-docking analysis of the protein-ligand interactions. Colour NCI plots are obtained from Atomistica online tool [33-35]. The temperature dependence of entropy (S), constant volume heat capacity (C_V) and constant-pressure heat capacity (C_P) was evaluated using the Shermo program.

Docking analysis

Selection of protein: The target protein was selected based on the biological activity predicted using the Way2-Drug PASS online tool. Human bactericidal/permeability-increasing protein (BPI; PDB ID: 1BP1) was retrieved from the RCSB Protein Data Bank for molecular docking. BPI is an antimicrobial protein that interacts with bacterial lipopolysaccharides and contributes to membrane disruption. However, the rationale for selecting 1BP1 should be supported by a specific predicted activity or literature evidence linking the title compound to BPI.

Preparation of protein: The 1BP1 structure was prepared by removing crystallographic water molecules and non-essential heteroatoms, followed by addition of hydrogen atoms, correction of structural deficiencies, charge assignment and energy minimization. The stereochemical quality of the structure was evaluated using a Ramachandran plot generated with PROCHECK/SAVES, with 85.1% of residues located in the most favoured regions [36]. However, this value is only moderate and should be discussed rather than presented as definitive evidence of protein suitability. The prepared structure was subsequently used for docking studies.

Preparation of ligand: The title compound was initially drawn using ChemSketch and converted into a three-dimensional structure using Avogadro. The geometry was optimized using the MMFF94 force field with the steepest-descent algorithm to minimize steric strain and obtain a stable conformation. The optimized structure was then exported in PDB format.

RESULTS AND DISCUSSION

Electronic structure analysis: The molecular structure $C_{20}H_{26}N_4O_2$ was optimized using the DFT/B3LYP method with the 6-31G(d) basis set. The compound is a derivative of 3-ethyl-1-hydroxy-2,6-diphenylpiperidin-4-one. Fig. 1 presents the optimized molecular structure together with its structural, electronic and energetic characteristics. The 2D (Fig. 1a) and optimized 3D (Fig. 1b) structures depict the substituted piperidine core, phenyl rings and hydroxy-containing hydrazone framework. The density of states (DOS) profile (Fig. 1c) displays the distribution of occupied and virtual molecular orbitals, with an energy separation between these states that provides insight into the electronic stability and reactivity of the molecule. The energy convergence profile (Fig. 1d) exhibits a pronounced decrease in total energy during the initial optimization steps, followed by stabilization near the fifth step. The optimization profile (Fig. 1e) approaches the target convergence criterion over the subsequent steps, confirming attainment of a stable optimized geometry. The optimized structure was subsequently used for the electronic and spectroscopic calculations. The atom numbering scheme is provided in Table-1, while the corresponding XYZ coordinates of the optimized structure are listed in Table-2.

Mulliken charge analysis: Mulliken population analysis is a commonly used approach for estimating partial atomic charges by partitioning the molecular electron density among individual atoms. Within the linear combination of atomic orbitals (LCAO) framework, the electron population associated with each atomic center and the overlap regions is used to obtain the net atomic charge. Such charge distribution provides insight into molecular polarity, chemical reactivity, hydrogen bonding propensity and electrostatic interactions [37]. The calculated Mulliken charges for all 52 atoms are listed in Table-3 and their graphical distribution is shown in Fig. 2. The calculated values exhibit substantial variation in the electro-

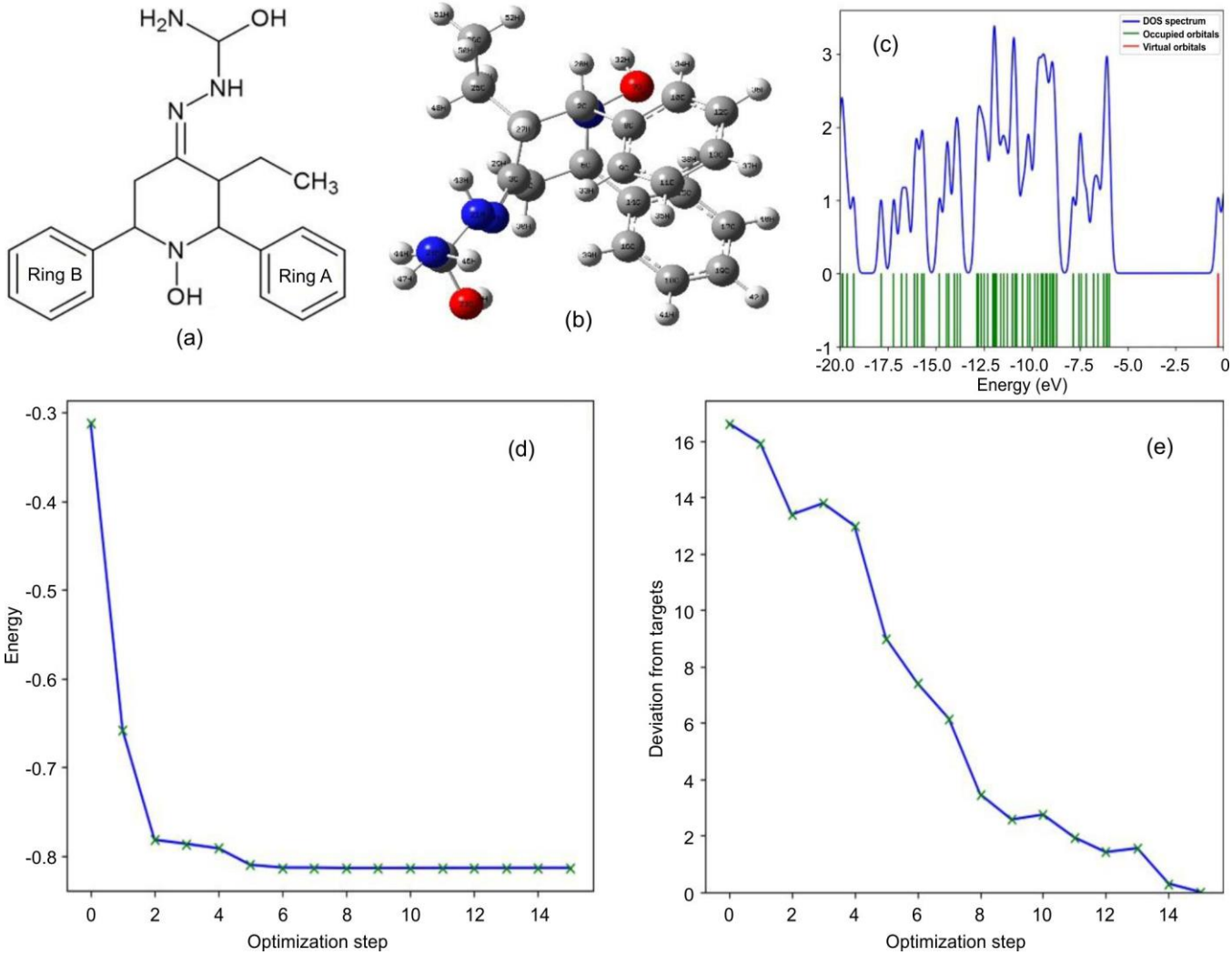

Fig. 1. (a) 2D, (b) 3D, (c) DOS, (d) convergence and (e) optimization of the titled molecule

TABLE-1
ATOM LIST OF THE OPTIMIZED MOLECULE

1	C	14	C	27	H	40	H
2	C	15	C	28	H	41	H
3	C	16	C	29	H	42	H
4	N	17	C	30	H	43	H
5	C	18	C	31	H	44	H
6	C	19	C	32	H	45	H
7	O	20	N	33	H	46	H
8	C	21	N	34	H	47	H
9	C	22	C	35	H	48	H
10	C	23	O	36	H	49	H
11	C	24	N	37	H	50	H
12	C	25	C	38	H	51	H
13	C	26	C	39	H	52	H

static environment of the molecule. The most negative charges occur at the heteroatomic centers 24N (-0.7139 a.u.), 23O (-0.6294 a.u.) and 7O (-0.5079 a.u.). These electron-rich sites can participate in hydrogen-bond acceptance and other electrostatic interactions. The largest positive charges are associated with 32H (0.4069 a.u.) and 45H (0.4028 a.u.), followed by 22C (0.3770 a.u.). The positive character of the hydrogen atoms is consistent with their bonding to electronegative nitrogen or oxygen centers, which can facilitate their participation as hydrogen-bond donor sites.

The carbon atoms display charge variations governed by their local bonding environments. Carbons within the phenyl rings and alkyl chains generally possess relatively small negative charges, as observed for 13C (-0.1249 a.u.). Carbon centers influenced directly by neighbouring heteroatoms exhibit higher positive character; 3C carries a charge of 0.3132 a.u. This redistribution of electron density contributes to the molecular polarization and dipole character. The hydrazone and hydroxyl containing regions possess pronounced charge separation and represent the principal electronically active sites for intermolecular interactions. Since the Mulliken charges were calculated from the optimized geometry, the obtained charge distribution corresponds to the energy-minimized molecular structure established through the convergence profiles in Fig. 1d-e.

Frontier orbital analysis: The calculated HOMO and LUMO energies of the title compound are -5.9468 and -0.2803 eV, respectively, giving a HOMO–LUMO energy gap (ΔE) of 5.6665 eV. The relatively large energy separation is associated with high kinetic stability and a lower tendency toward

TABLE-2
XYZ COORDINATES OF THE OPTIMIZED TITLED MOLECULE

Atom	Coordinates			Atom	Coordinates		
	X	Y	Z		X	Y	Z
C	-1.20393	1.53686	-0.18943	H	-1.67859	1.36405	0.78232
C	0.30549	1.80083	0.08710	H	0.39987	2.85633	0.36708
C	-1.38109	0.30121	-1.05768	H	-0.81411	0.95191	-3.00283
N	1.00166	1.74067	-1.21879	H	-0.63017	-0.78438	-2.74496
C	-0.49490	0.19288	-2.27562	H	1.47245	0.73129	-2.92359
C	0.99550	0.46628	-1.97179	H	2.37411	3.00020	-1.58889
O	2.35807	2.19242	-1.04894	H	-0.64386	-0.51670	1.39720
C	0.89365	1.00567	1.26122	H	2.55741	2.35749	1.45272
C	0.27927	-0.12645	1.81408	H	0.33834	-1.64939	3.33075
C	2.07225	1.47749	1.86160	H	3.54657	1.21277	3.40469
C	0.83459	-0.77368	2.92026	H	2.44280	-0.80701	4.35811
C	2.63160	0.82852	2.96071	H	3.67953	0.20847	-1.85176
C	2.01332	-0.30257	3.49636	H	0.10054	-1.96857	-0.89305
C	1.78871	-0.72484	-1.42064	H	5.04508	-1.70556	-1.09395
C	3.19133	-0.68420	-1.47532	H	1.45456	-3.87544	-0.15118
C	1.18149	-1.89396	-0.94207	H	3.93955	-3.76572	-0.23525
C	3.96058	-1.76384	-1.04489	H	-3.44784	0.33001	0.46457
C	1.95010	-2.98013	-0.51810	H	-4.88239	-1.20801	-0.76217
C	3.34197	-2.91946	-0.56435	H	-3.00107	-2.66261	-0.90430
N	-2.24686	-0.63083	-0.87444	H	-4.38801	-1.93388	2.00448
N	-3.09444	-0.59380	0.21779	H	-5.79958	-2.06194	1.17533
C	-4.21201	-1.53314	0.05322	H	-2.84649	2.44531	-1.28427
O	-3.69706	-2.81096	-0.23601	H	-1.26895	3.11505	-1.67519
N	-4.95653	-1.50120	1.27663	H	-2.82381	3.60046	0.94835
C	-1.89293	2.76694	-0.84413	H	-2.64870	4.75515	-0.38201
C	-2.16338	3.91789	0.13202	H	-1.24159	4.30144	0.58364

TABLE-3
MULLIKEN CHARGE OF THE TITLED MOLECULE

Atom	Charge (a.u.)	Atom	Charge (a.u.)	Atom	Charge (a.u.)	Atom	Charge (a.u.)
1C	-0.1734	14C	0.1651	27H	0.1475	40H	0.1231
2C	-0.0525	15C	-0.1639	28H	0.1420	41H	0.1255
3C	0.3132	16C	-0.1851	29H	0.1593	42H	0.1236
4N	-0.2405	17C	-0.1297	30H	0.1659	43H	0.3184
5C	-0.3360	18C	-0.1333	31H	0.1411	44H	0.1147
6C	-0.0483	19C	-0.1256	32H	0.4069	45H	0.4028
7O	-0.5079	20N	-0.3509	33H	0.1601	46H	0.3098
8C	0.1609	21N	-0.4387	34H	0.1310	47H	0.3122
9C	-0.1879	22C	0.3770	35H	0.1257	48H	0.1374
10C	-0.1620	23O	-0.6294	36H	0.1232	49H	0.1541
11C	-0.1367	24N	-0.7139	37H	0.1236	50H	0.1467
12C	-0.1307	25C	-0.2652	38H	0.1315	51H	0.1498
13C	-0.1249	26C	-0.4522	39H	0.1434	52H	0.1533

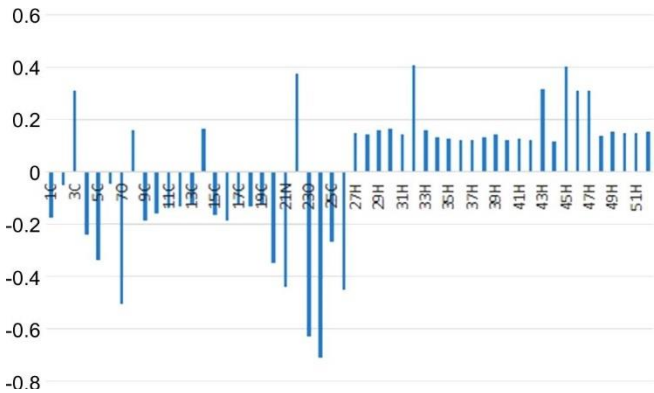

Fig. 2. Mulliken charge of the titled molecule

electronic excitation. Such an electronic configuration is consistent with the stable molecular framework obtained from geometry optimization. The calculated HOMO and LUMO energies, energy gap and associated global reactivity parameters are listed in Table-4, while their spatial distributions are shown in Fig. 3.

The HOMO is predominantly localized over the hydrazone linkage and central piperidine region, with appreciable electron density around the nitrogen-containing framework. These regions represent the electron-rich portion of the molecule and may participate in interactions involving electron donation. The LUMO is distributed mainly over the aromatic phenyl rings, providing electron-accepting regions within the

TABLE-4
HOMO-LUMO AND OTHER DERIVED REACTIVE PARAMETERS OF THE TITLED MOLECULE

Parameter	Charge (eV)
E_{HOMO}	-5.9468
E_{LUMO}	-0.2803
Energy gap (ΔE)	5.6665
Ionization potential (I)	5.9468
Electron affinity (A)	0.2803
Electronegativity (χ)	3.1136
Chemical potential (μ)	-3.1136
Chemical hardness (η)	2.8332
Chemical softness (S) (eV^{-1})	0.3530
Electrophilicity index (ω)	1.7109
Electron accepting capability (ω^+)	0.5082
Electron donating capability (ω^-)	3.6217
Net electrophilicity ($\Delta\omega^{\pm}$)	-3.1135
Global softness (s) (eV^{-1})	0.1765
$\Delta E_{Back\ donation}$	-0.7083
Nucleophilicity index (N) (eV^{-1})	0.5845
Additional electronic charge (ΔN_{max})	1.0990
Optical softness (σ_0) (eV^{-1})	0.1765

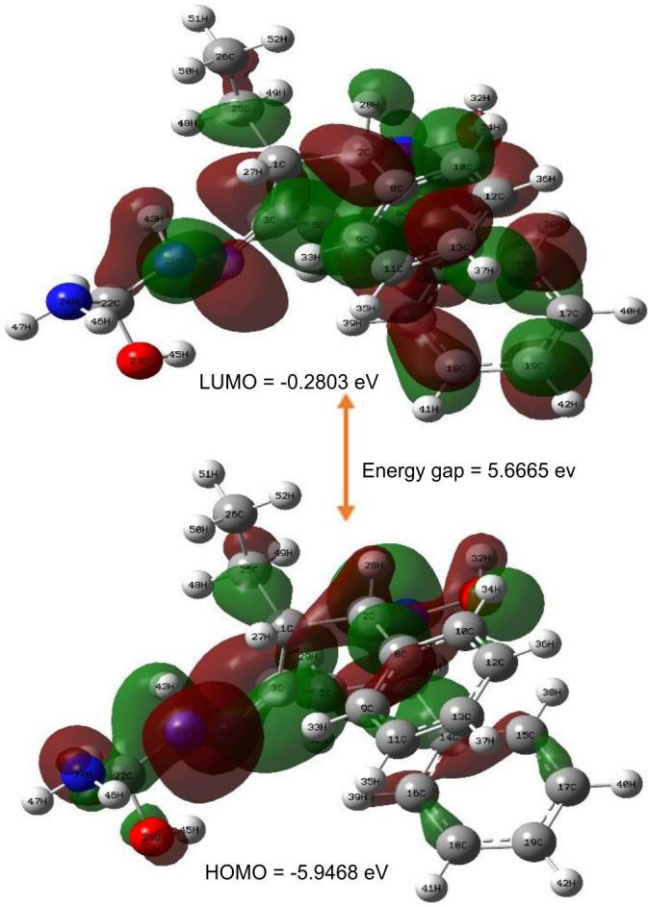

Fig. 3. HOMO-LUMO of titled molecule

molecular framework. The spatial separation between the frontier orbitals provides useful information on the preferred sites for charge-transfer interactions. The FMO distribution is consistent with the Mulliken charge analysis, in which the heteroatom-rich regions carry substantial negative charge. The combined orbital and charge distributions provide a molecular level description of the donor and acceptor characteristics of the title compound.

The global reactivity descriptors provide further quantitative information on the electronic behaviour of the molecule. The calculated chemical hardness (η) of 2.8332 eV and global softness (σ) of 0.3530 eV^{-1} are characteristic of a relatively hard molecular system. The sizeable hardness value is consistent with the calculated HOMO–LUMO separation and supports the high kinetic stability of the optimized structure. The electrophilicity index (ω) is 1.7109 eV, representing the tendency of the molecule to accept electronic charge. The electron donating power of 3.6217 eV is considerably higher than the electron-accepting power of 0.5082 eV, assigning a stronger electron-donor character to the molecule. This property is particularly relevant to the hydrazone and oxygen containing regions, where the calculated charge distribution identifies electron-rich centres.

The chemical potential (μ) of -3.1136 eV provides further insight into the electronic stability of the system. Its negative value is associated with a favourable electron distribution within the optimized molecular structure. The calculated optical softness of 0.1765 eV^{-1} provides an additional parameter for assessing the response of the molecular electron cloud to an external electric field. When considered alongside the frontier orbital energies and electronic distribution, this parameter supports further investigation of the compound's nonlinear optical (NLO) response and spectroscopic behaviour.

The optimization profiles presented in Fig. 1d-e establish the converged, energy-minimized geometry used for the FMO calculations. The FMO descriptors, orbital distributions and charge characteristics provide mutually consistent information on the electronic structure of the title compound. These results establish the hydrazone/piperidine region as an important electron-rich domain and the phenyl-containing region as a principal electron-accepting domain, providing a structural basis for interpreting its subsequent NLO and molecular docking properties.

Molecular electrostatic potential (MEP) analysis: The MEP surface of the title compound was calculated at the same DFT/basis-set level used for geometry optimization and is shown in Fig. 4. MEP analysis provides a three-dimensional representation of the electrostatic environment surrounding a molecule and is useful for locating regions involved in hydrogen

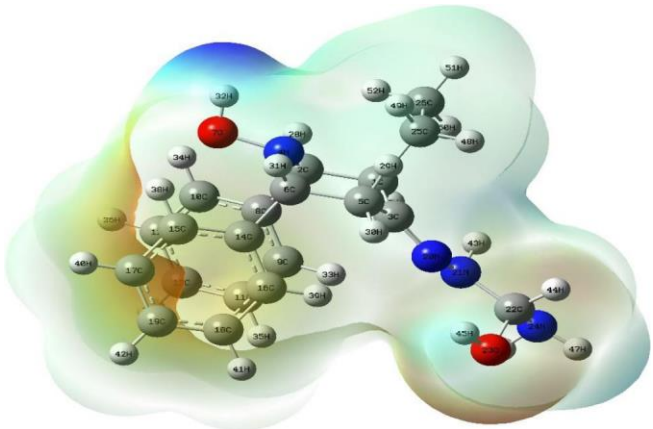

Fig. 4. MEP for the titled molecule

bonding, electrophilic-, nucleophilic-interactions and molecular recognition [38]. The calculated potential spans from -5.579 × 10^{-2} to +5.579 × 10^{-2} a.u., with the colour scale distinguishing electron-rich and electron-deficient regions. The MEP distribution complements the Mulliken charge and FMO analyses by correlating atomic charge characteristics with their spatial manifestation on the molecular surface.

The most negative potential regions occur around the oxygen atoms, particularly 23O and 7O, which appear as deep red zones on the MEP surface. These regions correspond to the electron-rich centres identified from the Mulliken population analysis and can participate in hydrogen-bond acceptance and other electrostatic interactions. The Mulliken charges of 23O (-0.6294 a.u.) and 7O (-0.5079 a.u.) support their pronounced electron-rich character. Nitrogen atom 24N, with the most negative Mulliken charge in the molecule (-0.7139 a.u.), belongs to another electron-rich region associated with the hydrazone framework. Its local MEP environment supports the role of the nitrogen-rich moiety in charge-dependent molecular interactions.

A distinct positive potential is observed around hydrogen atom 32H, which is attached to oxygen atom 7O. This region appears blue on the MEP surface and corresponds to the positive Mulliken charge of +0.4069 a.u. The O7–H32 group consequently represents a strongly polarized site with H-bond donor character. The spatial coincidence between the positive MEP region and the calculated atomic charge provides a consistent description of the hydroxyl group as an important site for intermolecular hydrogen bonding. Such polarization can contribute to molecular recognition through interactions with electronegative residues in biological targets.

The aromatic phenyl rings and ethyl substituent are predominantly covered by green to yellow-green regions, corresponding to relatively moderate electrostatic potentials. The phenyl rings retain a comparatively nonpolar character associated with delocalized π-electron density, while the ethyl group contributes little to the extreme positive or negative regions of the MEP surface. Carbon atoms located near electronegative heteroatoms display greater positive character. In particular, 22C (+0.3770 a.u.) and 3C (+0.3132 a.u.) are associated with regions of enhanced positive potential near the functional groups. Their charge distribution can be related to the inductive influence of neighbouring nitrogen and oxygen atoms.

The MEP surface establishes a clear correspondence between the calculated atomic charges and the spatial distribution of electrostatic potential. The red regions centred on 23O and 7O, the electron-rich nitrogen containing region around 24N, and the blue region associated with O7–H32 define the principal polar sites of the molecule. These features complement the FMO results, where the hydrazone and piperidine regions contribute substantially to the HOMO distribution. The MEP characteristics were obtained from the optimized, energy-minimized geometry established through the convergence profiles in Fig. 1d-e, providing a consistent structural basis for interpreting the molecule's reactive sites and intermolecular interactions.

Non-linear optical analysis: The NLO properties of the title molecule were evaluated using the B3LYP/6-31G(d) level of theory and the calculated dipole moment, polarizability and first-order hyperpolarizability values are presented and discussed. The values are shown in Table-5. The desired parameters are calculated by the following equations:

$$\mu = \sqrt{\mu_x^2 + \mu_y^2 + \mu_z^2} \quad (1)$$

$$\alpha_{total} = \frac{\alpha_{xx} + \alpha_{yy} + \alpha_{zz}}{3} \quad (2)$$

$$\Delta\alpha = \frac{1}{\sqrt{2}}\sqrt{\begin{matrix}(\alpha_{xx} - \alpha_{yy})^2 + (\alpha_{yy} - \alpha_{zz})^2 + \\ (\alpha_{zz} - \alpha_{xx})^2 + 6(\alpha_{xy}^2 + \alpha_{xz}^2 + \alpha_{yz}^2)\end{matrix}} \quad (3)$$

$$\beta_{Tot} = \sqrt{\beta_x^2 + \beta_y^2 + \beta_z^2} \quad (4)$$

where

$$\beta_x = \beta_{xxx} + \beta_{xyy} + \beta_{xzz}$$

$$\beta_y = \beta_{yyy} + \beta_{xxy} + \beta_{yzz}$$

$$\beta_z = \beta_{zzz} + \beta_{xxz} + \beta_{yyz}$$

$$\beta_{vec} = \frac{3}{5}\sqrt{\begin{matrix}(\beta_{xxx} + \beta_{xyy} + \beta_{xzz})^2 + (\beta_{yyy} + \beta_{xxy} + \beta_{yzz})^2 + \\ (\beta_{zzz} + \beta_{xxz} + \beta_{xyz})^2\end{matrix}} \quad (5)$$

$$\beta(HRs) = \sqrt{\beta_{zzz}^2 + \beta_{zxx}^2} \quad (6)$$

$$DR = \frac{\beta_{zzz}^2}{\beta_{zxx}^2} \quad (7)$$

TABLE-5
NLO DETAILS FOR THE TITLED MOLECULE

Dipole-moment (D)		Static first order hyperpolarizability (a.u.)	
μ_x	-0.1181487	β_{xxx}	-23.308067
μ_y	1.0161707	β_{xxy}	9.8001287
μ_z	-0.4183185	β_{xyy}	-7.4822386
μ (Debye)	1.096	β_{yyy}	-17.3622797
Static polarizability (a.u.)		β_{xxz}	-81.1106672
α_{xx}	267.5424874	β_{xyz}	-6.4765077
α_{xy}	9.4310386	β_{yyz}	-53.2328183
α_{yy}	234.4745206	β_{xzz}	39.0674575
α_{xz}	6.0899464	β_{yzz}	7.3140386
α_{yz}	30.2655566	β_{zzz}	13.7838435
α_{zz}	193.7697515	β_{Tot} (a.u.)	120.8436
α_{tot} (a.u.)	231.9281	β_{Tot} (e.s.u)	1.044 × 10^{-30}
α_{tot} (esu)	34.367× 10^{-24}	β_{Vec}(a.u.)	72.5062
Δα (a.u.)	65.41	DR	-3.8619
Δα (e.s.u)	9.692 × 10^{-24}	β(HRs) (a.u.)	46.81
		β(HRs) (esu)	0.404 × 10^{-30}

The computational analysis of the target molecule reveals a total dipole moment of 1.096 Debye, primarily driven by the *y*-axis component (1.016 D). The linear polarizability (α_{tot}) was calculated at 34.367 × 10^{-24} esu, while the first-order hyperpolarizability (β_{vec}) reached 1.044 × 10^{-30} esu. The calculated NLO response is strongly influenced by the β tensor component (-120.56 a.u.), which represents a pronounced longitudinal electronic response along the hydrazone-linked

framework. The depolarization ratio (DR) of -3.8619 is associated with an anisotropic electronic environment and provides further insight into the direction-dependent polarization response of the molecule.

When compared to the standard NLO reference material, Urea (β_{urea} = 0.3728 ×10^{-30} esu), the target molecule exhibits a hyperpolarizability value approximately 2.8 times higher. This superior NLO response is attributed to the extended π-conjugation and the presence of electronegative heteroatoms (nitrogen & oxygen), which promote stronger intramolecular charge transfer compared to the smaller urea molecule. Consequently, the high β_{vec} and β(HRS) values categorize this organic framework as a promising candidate for the development of high-performance nonlinear optical materials and frequency-doubling devices.

While the calculated first-order hyperpolarizability (β_{tot} 1.044 × 10^{-30} esu) is compared with the standard reference urea (2.8 times higher), its practical significance lies in overcoming the classic nonlinearity-transparency trade-off inherent in organic NLO materials. Highly optimized, extended π-conjugated D–π–A chromophores frequently exhibit larger β_{tot} values, but they typically suffer from narrow energy gaps, intense absorption in the visible region and poor thermal/kinetic stability. In contrast, the title compound exhibits a remarkably wide HOMO-LUMO gap of 5.6665 eV, ensuring excellent deep-UV/Visible optical transparency and high chemical stability. The structural integration of the rigid 2,6-diphenylpiperidin-1-ol core with the flexible hydrazone linkage effectively induces localized asymmetric charge transfer without severely compromising the optical bandgap. Therefore, this molecule serves as a highly efficient, high-transparency NLO candidate suitable for optoelectronic applications where both frequency conversion efficiency and high laser-induced damage thresholds are simultaneously required.

Fukui function analysis: Electron population differences obtained from natural population analysis (NPA) or Mulliken population analysis (MPA) for the neutral, anionic and cationic states can be used to quantitatively rank atomic sites according to their relative chemical reactivity and selectivity.

The individual atomic charges calculated by NPA and MPA have been used to determine Fukui function. Fukui function is a local reactivity descriptor defined as [39,40]:

$$f(\vec{r}) = \left(\frac{\partial \rho(\vec{r})}{\partial N}\right)_{v(\vec{r})} = \left(\frac{\partial \mu}{\partial \upsilon(\vec{r})}\right)_{N} \quad (8)$$

which may be approximated as follows due to the discontinuities in the above derivatives.

$$f^{+}(\vec{r}) = \rho_{N+1}(\vec{r}) - \rho_{N}(\vec{r}) \text{ for nucleophilic attack} \quad (9)$$

$$f^{-}(\vec{r}) = \rho_{N}(\vec{r}) - \rho_{N-1}(\vec{r}) \text{ for electrophilic attack} \quad (10)$$

$$f^{0}(\vec{r}) = (\rho_{N+1}(\vec{r}) - \rho_{N-1}(\vec{r}))/2 \text{ for radical attack} \quad (11)$$

Eqn. 12 provides the dual descriptor Δf(r), which is defined as the difference between the nucleophilic and electrophilic Fukui function [41]:

$$\Delta f(r) = [f^{+} - f^{-}] \quad (12)$$

Fukui function analysis using natural population analysis (NPA) and Mulliken population analysis (MPA) was performed to identify the preferred reactive sites within the 52-atom molecular framework (Table-6). The NPA results show appreciable Fukui indices at the nitrogen centres associated with the hydrazone and amine functionalities. Among these, 21N (0.2298 a.u.) and 4N (0.1874 a.u.) possess prominent values, identifying them as important sites for nucleophilic attack. Carbon atoms 1C (0.2531 a.u.) and 16C (0.1593 a.u.) exhibit notable values and may undergo significant electron-density redistribution during chemical interactions. The corresponding plots in Fig. 5a-b illustrate the changes in electron populations among the anionic, neutral and cationic states.

Hydrogen atom 32H exhibits an NPA Fukui index of 0.0788 a.u. and represents a reactive site within the hydroxyl-containing region. Its Fukui response is consistent with the positive electrostatic potential observed around this hydrogen in the MEP analysis, supporting its possible involvement in hydrogen-bond donation and proton-transfer interactions. The MPA results follow a similar trend, although differences in numerical values arise from the two population-analysis schemes. A localized contribution from 46H (0.0191 a.u.) is observed in the MPA data.

The analysis identifies 24N as an important site for electrophilic attack. The NPA calculations assign a relatively high Fukui response to 24N across the anionic, neutral and cationic states (Fig. 6). The MPA results provide the same qualitative assignment, with 24N retaining a high Fukui value across these charge states. The agreement between NPA and MPA supports the assignment of the nitrogen-rich hydrazone region as a principal reactive domain. These findings complement the Mulliken charge and MEP results, with the nitrogen containing core representing a major site for chemical interactions and selected carbon and hydrogen atoms contributing to secondary reactive regions.

The Fukui indices calculated using NPA and MPA provide a quantitative assessment of the preferred reactive sites in the anionic, neutral and cationic states of the molecule. For the

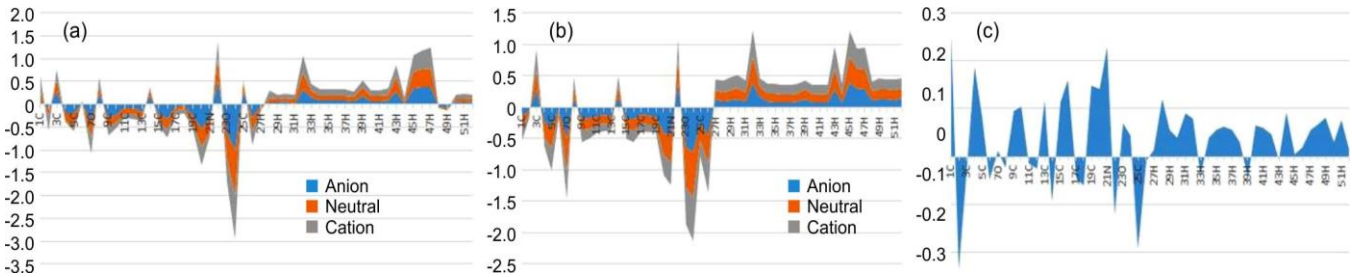

Fig. 5. (a) NPA, (b) MPA and (c) Δf(r) values obtained for the titled molecule

TABLE-6
NPA AND MPA VALUES ALONG WITH Δ(f) VALUES FOR THE TITLED MOLECULE

Atom	NPA (a.u.)				MPA (a.u.)		
	Anion	Neutral	Cation	Δf(r)	Anion	Neutral	Cation
1C	0.0937	0.1693	0.3468	0.2531	-0.1546	-0.1734	-0.1956
2C	-0.1054	-0.1377	-0.3415	-0.2361	-0.0471	-0.0525	-0.0789
3C	0.2691	0.2676	0.2260	-0.0431	0.2718	0.3132	0.3492
4N	-0.1916	-0.2098	-0.0042	0.1874	-0.2378	-0.2405	-0.1521
5C	-0.2107	-0.2383	-0.1265	0.0842	-0.3132	-0.3360	-0.3580
6C	0.0172	0.0503	-0.0316	-0.0488	-0.0419	-0.0483	-0.0817
7O	-0.3620	-0.3781	-0.3493	0.0127	-0.5100	-0.5079	-0.4557
8C	0.2252	0.1653	0.2016	-0.0236	0.1521	0.1609	0.1681
9C	-0.2959	-0.1959	-0.2015	0.0944	-0.1844	-0.1879	-0.1776
10C	-0.2341	-0.1555	-0.1292	0.1049	-0.1796	-0.1620	-0.1570
11C	-0.0858	-0.1056	-0.0996	-0.0138	-0.1481	-0.1367	-0.1295
12C	-0.0912	-0.1031	-0.1171	-0.0259	-0.1266	-0.1307	-0.1265
13C	-0.1880	-0.1181	-0.0700	0.118	-0.1465	-0.1249	-0.1152
14C	0.1802	0.1179	0.0847	-0.0955	0.1595	0.1651	0.1703
15C	-0.2165	-0.1407	-0.1025	0.114	-0.1810	-0.1639	-0.1618
16C	-0.3267	-0.2270	-0.1674	0.1593	-0.1828	-0.1851	-0.1819
17C	-0.0542	-0.0733	-0.1006	-0.0464	-0.1257	-0.1297	-0.1264
18C	-0.0356	-0.0678	-0.0962	-0.0606	-0.1446	-0.1333	-0.1290
19C	-0.2502	-0.1637	-0.1011	0.1491	-0.1474	-0.1256	-0.1182
20N	-0.5289	-0.4072	-0.3884	0.1405	-0.4221	-0.3509	-0.3132
21N	-0.3203	-0.2878	-0.0905	0.2298	-0.4387	-0.4387	-0.3664
22C	0.5214	0.4729	0.3985	-0.1229	0.3908	0.3770	0.3492
23O	-0.5999	-0.5709	-0.5302	0.0697	-0.6482	-0.6294	-0.5972
24N	-1.0115	-0.9933	-0.9678	0.0437	-0.7168	-0.7139	-0.7045
25C	0.2727	0.1953	0.0775	-0.1952	-0.2513	-0.2652	-0.2767
26C	-0.2916	-0.3014	-0.3018	-0.0102	-0.4448	-0.4522	-0.4593
27H	-0.0686	-0.0588	-0.0540	0.0146	0.1225	0.1475	0.1727
28H	0.0365	0.0985	0.1577	0.1212	0.0931	0.1420	0.1858
29H	0.0297	0.0820	0.0855	0.0558	0.1056	0.1593	0.2061
30H	0.0561	0.0786	0.0964	0.0403	0.1316	0.1659	0.2095
31H	0.0254	0.0753	0.1149	0.0895	0.0833	0.1411	0.1920
32H	0.3213	0.3622	0.4001	0.0788	0.3811	0.4069	0.4404
33H	0.1715	0.1386	0.1317	-0.0398	0.1552	0.1601	0.1435
34H	0.0877	0.1079	0.1269	0.0392	0.0901	0.1310	0.1544
35H	0.0783	0.1106	0.1330	0.0547	0.0814	0.1257	0.1585
36H	0.0774	0.1086	0.1401	0.0627	0.0729	0.1232	0.1641
37H	0.0766	0.1085	0.1319	0.0553	0.0671	0.1236	0.1669
38H	0.0753	0.0942	0.1059	0.0306	0.0914	0.1315	0.1513
39H	0.1943	0.1758	0.1500	-0.0443	0.1354	0.1434	0.1375
40H	0.0703	0.1027	0.1354	0.0651	0.0732	0.1231	0.1617
41H	0.0710	0.1047	0.1304	0.0594	0.0808	0.1255	0.1564
42H	0.0917	0.1188	0.1372	0.0455	0.0675	0.1236	0.1638
43H	0.2858	0.2977	0.2790	-0.0068	0.2860	0.3184	0.3585
44H	0.0114	0.0470	0.1035	0.0921	0.0780	0.1147	0.1750
45H	0.3542	0.3516	0.3599	0.0057	0.3970	0.4028	0.4147
46H	0.3792	0.3857	0.3983	0.0191	0.3000	0.3098	0.3281
47H	0.3847	0.4090	0.4393	0.0546	0.2855	0.3122	0.3455
48H	-0.0589	-0.0271	0.0079	0.0668	0.1162	0.1374	0.1603
49H	-0.0829	-0.0483	-0.0028	0.0801	0.1351	0.1541	0.1637
50H	0.0525	0.0677	0.0823	0.0298	0.1310	0.1467	0.1640
51H	0.0362	0.0745	0.1118	0.0756	0.1141	0.1498	0.1860
52H	0.0638	0.0707	0.0798	0.0160	0.1440	0.1533	0.1654

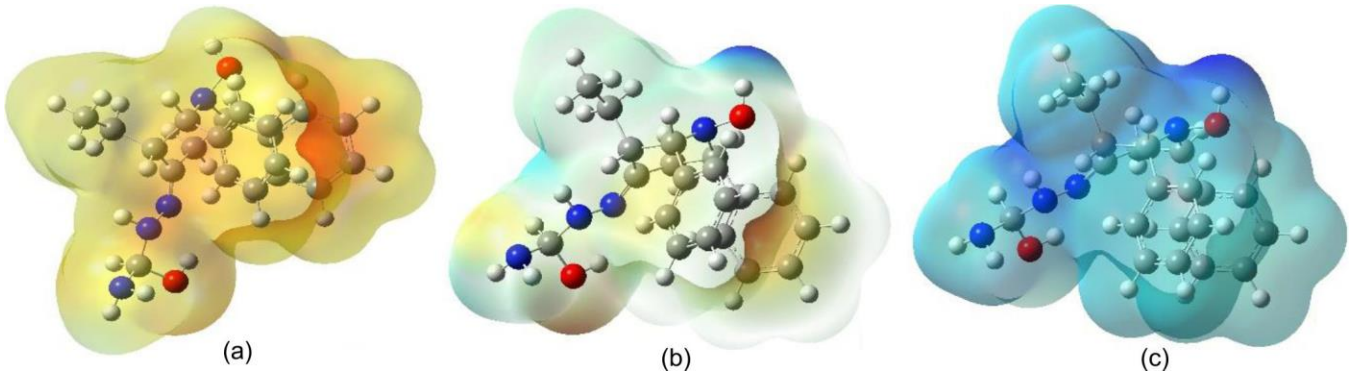

Fig. 6. MEP images for the cationic, neutral and anionic species of the titled molecule

anion, the NPA-based electrophilic attack sequence is 24N > 23O > 20N > 7O > 16C > 21N, while the nucleophilic attack sequence is 22C > 47H > 46H > 45H > 32H. For the neutral molecule, the corresponding sequences are 24N > 23O > 20N > 7O > 26C for electrophilic attack and 22C > 47H > 46H > 32H > 45H for nucleophilic attack. In the cationic state, the electrophilic attack preference follows 24N > 23O > 20N > 7O > 2C > 26C, whereas the nucleophilic attack sequence is 47N > 32H > 22C > 46H > 45H > 1C. The recurrent position of 24N and 23O among the principal electrophilic-attack sites identifies the nitrogen- and oxygen-rich regions as important electron-accepting interaction centres.

The MPA results provide comparable trends with some changes in the relative ranking of individual atoms. For the anion, electrophilic attack follows 24N > 23O > 7O, while nucleophilic attack follows 45H > 22C > 32H > 46H. For the neutral species, the electrophilic sequence is 24N > 23O > 7O > 26C > 21N, and the nucleophilic sequence is 32H > 45H > 22C > 43H > 3C > 47H > 46H. For the cation, electrophilic attack follows 24N > 23O > 26C > 7O, whereas nucleophilic attack follows 32H > 45H > 43H > 22C > 3C > 47H > 46H. The repeated occurrence of 24N as the highest-ranked electrophilic site across the charge states provides a consistent assignment of this nitrogen centre as a chemically active region.

Natural bond orbital (NBO) analysis: For the target organic molecule, NBO analysis is essential for identifying the specific resonance transitions that govern its stability and reactivity. The analysis focuses on the delocalization of electrons within the aromatic phenyl rings and the critical hydrazone-piperidine linkage, where nitrogen lone pairs typically participate in strong hyperconjugative interactions with adjacent antibonding orbitals. These interactions not only stabilize the molecular framework but also directly influence the electronic properties observed in the HOMO-LUMO gap and the NLO response. By examining the occupancy and energy of these natural orbitals, researchers can pinpoint the exact origin of the molecule's chemical behaviour and its potential for specific biological or synthetic interactions. For this molecule, NBO is investigated at the same level of the theory and reported in Table-7.

The molecule is stabilized with the transition of stabilization energy of 6.00 kcal/mol from the donor system of σ (C3-C5) to σ* (N20-N21). Similarly, The NBO analysis reveals several significant donor–acceptor interactions contributing to the electronic stabilization of the molecule. The acceptor orbital σ* (C22–N24) receives 4.14 kcal/mol from the donor orbital σ(O23–H45). Pronounced π→π* delocalization occurs between the aromatic systems, with stabilization energies of 20.50 and 20.53 kcal/mol for π(C10–C12)→π*(C11–C13) and π(C15–C17)→π*(C18–C19), respectively. The lone-pair orbitals contribute substantially to the stabilization of the molecular framework. The interaction LP(1) N20→σ*(C1–C3) has a stabilization energy of 12.28 kcal/mol, while LP(1) N24→σ*(C22–023) contributes 13.27 kcal/mol. The oxygen lone pair, LP(2) O23, participates in two charge-transfer interactions with σ*(N21–C22) and σ*(C22–H44), with stabilization energies of 7.53 and 7.24 kcal/mol, respectively. A stronger interaction is observed for LP(1) N21→σ*(C3–N20), with a stabilization energy of 19.44 kcal/mol. A hydrogen bond associated interaction is identified between LP(1) N20 and the antibonding orbital σ*(O23–H45), with a stabilization energy of 4.60 kcal/mol. These donor–acceptor interactions, spanning σ→σ*, π→π* and lone-pair-mediated charge transfer, contribute to the electronic stabilization and delocalization of the molecular framework.

Non-covalent interaction (NCI) analysis: For the titled molecule under investigation, NCI interactions were studied under the same basis set with the help of Multiwfn 3.8 tool. The outcome was generated and reproduced in Fig. 7. It is defined as follows:

$$RDG(r) = \frac{1}{2(3\pi^2)^{1/3}} \frac{|\nabla\rho(r)|}{\rho(r)^{4/3}} \quad (13)$$

The provided NCI analysis reveals a complex network of non-covalent interactions within the molecular system, visualized through both the scatter plot (a) and the spatial isosurfaces (b):

- **Strong attractive interactions (hydrogen bonding):** The RDG-sign(λ_2)ρ scatter plot exhibits distinct blue spikes extending toward the baseline (RDG ≈ 0) within the negative sign(λ_2)ρ region (-0.04 to -0.02 a.u.), characteristic of attractive non-covalent interactions [41]. These features correspond to the hydrogen-bonding interactions identified in the molecular structure and appear as blue to cyan regions in the three-dimensional NCI surface. The presence of these attractive interactions contributes to the stabilization of the optimized molecular conformation.

TABLE-7
SECOND-ORDER PERTURBATION THEORY ANALYSIS OF THE
FOCK MATRIX IN THE NBO BASIS FOR THE TITLED MOLECULE

Type	Donor NBO (i)	ED/e (a.u.)	Type	Acceptor NBO(j)	ED/e (a.u.)	E(2) (kcal/mol)	E(j)-E(i) (a.u.)	F(i,j) (a.u.)
σ	C3-C5	1.9719	σ*	N20-N21	0.0232	6.00	0.99	0.069
π	C8-C9	1.6591	π*	C10-C12	0.3185	20.20	0.28	0.068
π	C8-C9	1.6591	π*	C11-C13	0.3304	20.34	0.28	0.067
π	C10-C12	1.6673	π*	C8-C9	0.3465	19.74	0.28	0.067
π	C10-C12	1.6673	π*	C11-C13	0.3304	20.50	0.28	0.068
π	C11-C13	1.6673	π*	C8-C9	0.3465	20.25	0.29	0.068
π	C11-C13	1.6673	π*	C10-C12	0.3185	19.78	0.28	0.067
π	C14-C16	1.6589	π*	C15-C17	0.3180	20.14	0.28	0.068
π	C14-C16	1.6589	π*	C18-C19	0.3312	20.42	0.28	0.068
π	C15-C17	1.6673	π*	C14-C16	0.3462	19.81	0.28	0.067
π	C15-C17	1.6673	π*	C18-C19	0.3312	20.53	0.28	0.068
π	C18-C19	1.6679	π*	C14-C16	0.3462	20.21	0.29	0.068
π	C18-C19	1.6679	π*	C15-C17	0.3180	19.75	0.28	0.067
σ	C22-N24	1.9902	σ*	O23-H45	0.0229	1.36	1.19	0.036
σ	O23-H45	1.9830	σ*	N21-C22	0.0574	1.07	1.03	0.030
σ	O23-H45	1.9830	σ*	C22-N24	0.0309	4.14	1.08	0.060
LP(1)	N4	1.9191	σ*	C2-C8	0.0420	8.18	0.73	0.070
LP(1)	N4	1.9191	σ*	C6-C14	0.0438	8.31	0.73	0.070
LP(1)	N20	1.9120	σ*	C1-C3	0.0444	12.28	0.78	0.088
LP(1)	N20	1.9120	σ*	O23-H45	0.0229	4.60	0.81	0.056
LP(1)	N21	1.8401	π*	C3-N20	0.1791	19.44	0.34	0.073
LP(2)	O23	1.94655	σ*	N21-C22	0.0574	7.53	0.62	0.061
LP(2)	O23	1.94655	σ*	C22-H44	0.0500	7.24	0.73	0.065
LP(1)	N24	1.9275	σ*	C22-O23	0.0670	13.27	0.62	0.081

E(2) is the energy of hyper conjugative interaction (stabilization energy).
E(j)-E(i) is the energy difference between donor and acceptor i and j NBO orbitals.
F(i,j) is the Fock matrix element between i and j NBO orbitals.
ED/e is the electron density of donor and acceptor NBO orbitals.
LP(n)A is a valence lone pair orbital (n) on A atom.

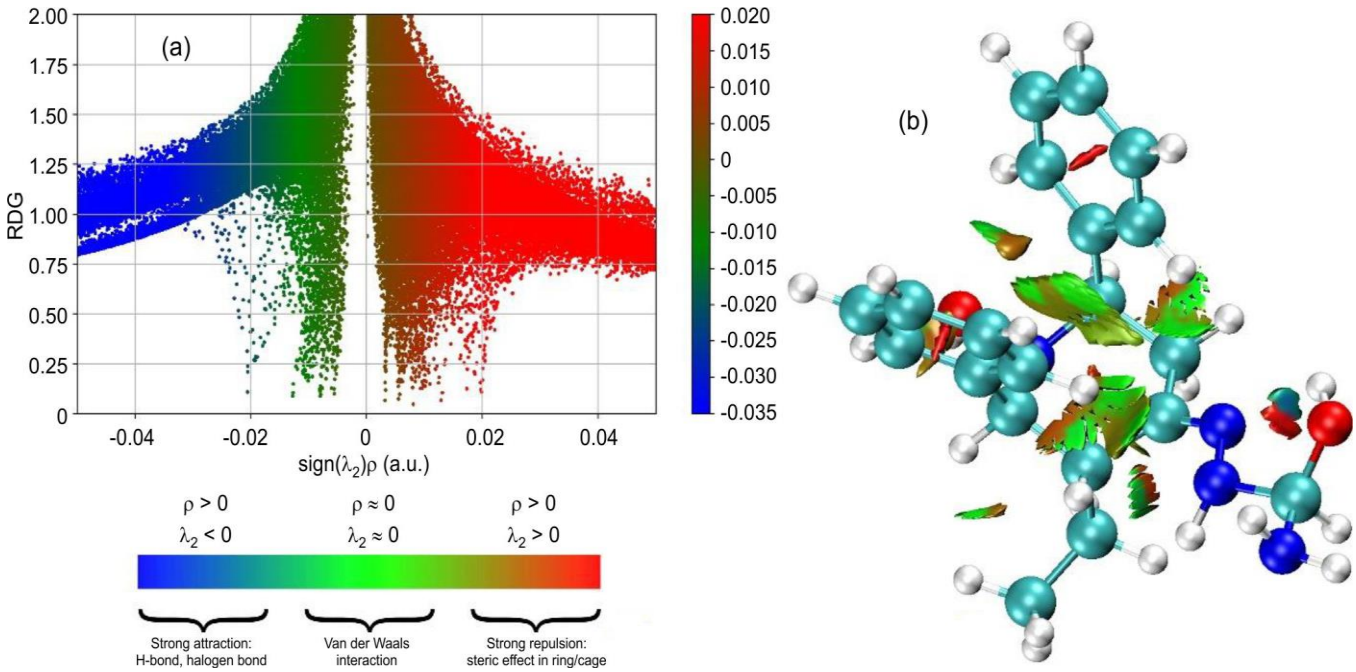

Fig. 7. (a) The NCI (b) iso-surface images of the titled molecule

- **Van der Waals interactions:** The central green region of the scatter plot, where sign(λ_2)ρ is close to zero, represents weak van der Waals forces [41]. In the 3D isosurface map, these are visible as broad, green-coloured 'sheets' located between various functional groups and aromatic rings, suggesting a high degree of dispersive stabilization across the molecular framework.
- **Steric repulsion:** On the right side of scatter plot (positive sign(λ_2)ρ values), the red spikes signify strong steric repulsion [41]. These correlate with the red/orange blobs located in the center of the ring systems and crowded regions in the 3D plot, highlighting the 'steric strain' or cage effects inherent in the cyclic parts of the structure.

Aromaticity analysis: Aromaticity was evaluated for the two phenyl rings using established aromaticity indices based on structural and electronic parameters [42-45]. The calculated aromaticity descriptors are shown in Table-8. Both phenyl rings exhibit pronounced aromatic character, with HOMA values of 0.971580 (ring 1) and 0.971750 (ring 2), which are close to the ideal value of 1. The Bird indices of 96.637421 and 96.692061 further support their high aromaticity, while the low PDI and FLU values (~0.001) indicate minimal disruption of aromatic electron delocalization by the substituents.

Shaded surface map with a projection of localized orbital locator (LOL) analysis: The localized orbital locator (LOL) was employed to visualize electron localization and distinguish regions associated with covalent bonds, lone pairs and electron delocalization within the molecule [46]. High LOL values correspond to strongly localized electron regions, while lower values represent higher electron delocalization:

$$LOL(r) = \frac{\tau(r)}{1+\tau(r)} \quad (14)$$

LOL analysis was performed using Multiwfn 3.8 and the corresponding surface maps are shown in Fig. 8. The colour-coded maps show pronounced electron localization around the covalent bonds of the aromatic rings and piperidine core, while distinct high-localization regions occur around the nitrogen and oxygen atoms due to their lone-pair electrons. The side-chain view displays localized electron density along the ethyl bonds, with comparatively diffuse regions around the hydrogen atoms. These LOL distributions are obtained from the optimized, energy-minimized molecular geometry

TABLE-8
VARIOUS AROMATICITIES FOR THE TITLED MOLECULE

Phenyl ring	PDI	FLU	PLR	HOMA	BIRD
A	0.099612	0.001097	0.607333	0.971580	96.637421
B	0.099645	0.001077	0.607847	0.971750	96.692061

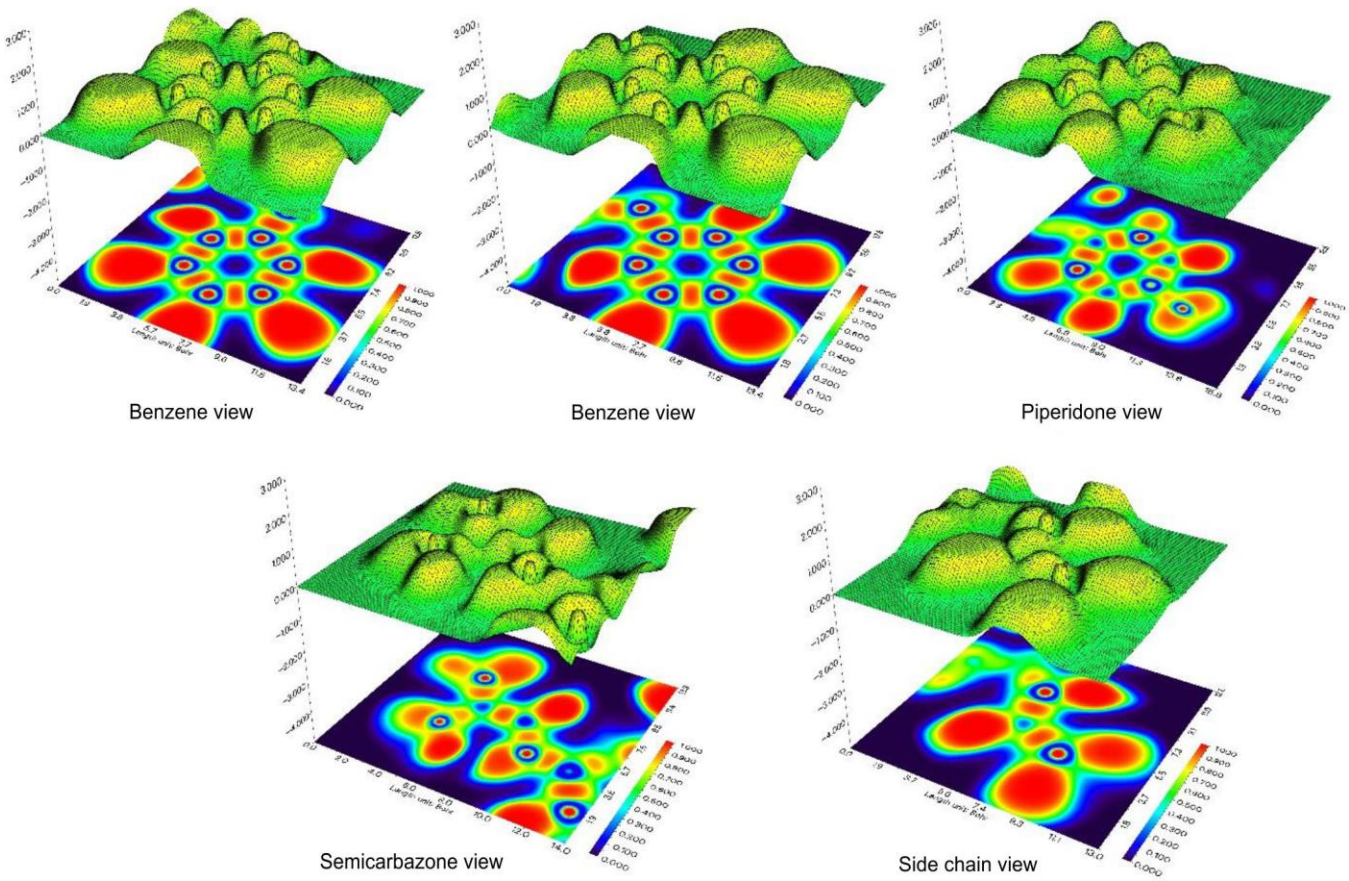

Fig. 8. Shaded surface map with a projection of LOL for the titled molecule

and provide a spatial representation of the ground-state electron localization within the molecule.

Laplacian electron density and Mayer bond order: The Laplacian of electron density ($\nabla^2\rho(r)$) provides information on regions of electron-density concentration and depletion within a molecule, with negative and positive values associated with charge concentration and depletion, respectively [47]. Mayer bond order (MBO) offers a quantitative measure of bond strength and electron sharing derived from the molecular density matrix [48]. These descriptors were calculated using Multiwfn 3.8 to examine the bonding characteristics and electronic distribution of the title compound. The MBO values are listed in Table-9, while the Laplacian electron-density distribution is shown in Fig. 9.

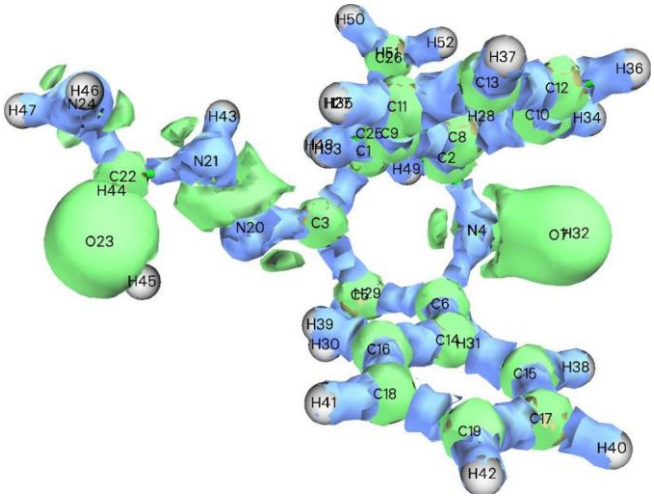

Fig. 9. Laplacian electron density for the titled molecule

The Laplacian map displays pronounced electron-density concentration around the heteroatom-rich regions, particularly O23, N20 and N21. The MBO values provide quantitative support for the bonding characteristics of the molecular framework. The phenyl rings exhibit MBO values ranging from 1.4208 for 14C–15C to 1.4560 for 18C–19C, consistent with delocalized aromatic bonding. The hydrazone linkage, represented by the 3C–20N bond, has a comparatively high MBO of 1.6852, supporting substantial multiple-bond character. In contrast, the 22C–24N (1.0738) and 21N–22C (0.9010) bonds possess values consistent with predominantly single-bond character.

The O7–H32 and O23–H45 bonds have MBO values of 0.7848 and 0.7362, respectively, consistent with their polar covalent character and potential involvement in hydrogen-bond interactions. The Laplacian and MBO results provide complementary information on electron-density distribution and bond character within the molecule. These calculations were performed using the optimized geometry obtained after convergence of the energy and optimization profiles (Fig. 1d–e) providing a consistent structural basis for the bonding analysis

Scanning tunneling microscopy (STM) analysis: STM enables atomic-scale surface imaging through quantum tunneling between a conducting tip and sample, while also providing topographic and local electronic-state information (LDOS) [49,50]. This property is studied for the tested molecule with the help of Multiwfn 3.8 software. The simulated STM images for the title molecule are shown in Fig. 10.

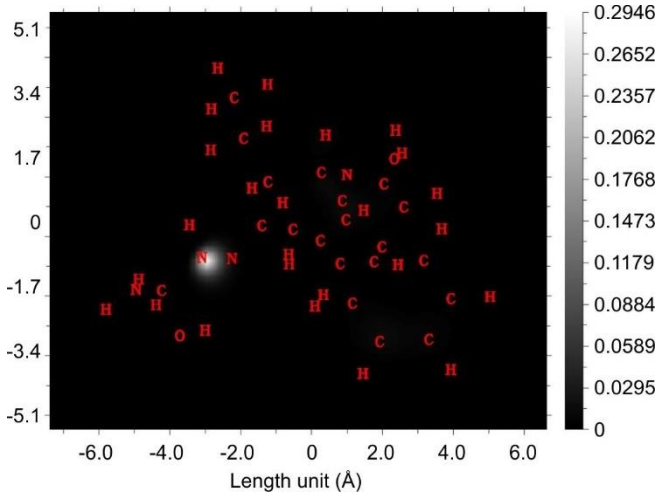

Fig. 10. STM image for the molecule under investigation

To visualize the spatial distribution of the FMOs and simulate the local electronic topography of the title compound, STM simulations were performed using the Tersoff-

TABLE-9
MAYER BOND ORDER DETAILS FOR THE OPTIMIZED TITLED MOLECULE

Atom set	MBO	Atom set	MBO	Atom set	MBO	Atom set	MBO
1C-2C	0.9457	5C-30H	0.9216	13C-37H	0.9304	21N-22C	0.9010
1C-3C	0.9728	6C-14C	0.9435	14C-15C	1.4208	21N-43H	0.8036
1C-25C	0.9688	6C-31H	0.9211	14C-16C	1.4398	22C-23O	0.9896
1C-27H	0.9051	7O-32H	0.7848	15C-17C	1.4423	22C-24N	1.0738
2C-4N	0.9193	8C-9C	1.4338	15C-38H	0.9158	22C-44H	0.9204
2C-8C	0.9373	8C-10C	1.4215	16C-18C	1.4318	23O-45H	0.7362
2C-28H	0.9109	9C-11C	1.4348	16C-39H	0.9055	24N-46H	0.8458
3C-5C	1.0001	9C-33H	0.9014	17C-19C	1.4412	24N-47H	0.8537
3C-20N	1.6852	10C-12C	1.4422	17C-40H	0.9303	25C-26C	1.0132
3C-21N	0.0829	10C-34H	0.9159	18C-19C	1.4560	25C-48H	0.9385
4N-6C	0.9225	11C-13C	1.4551	18C-41H	0.9296	25C-49H	0.9267
4N-7O	0.9136	11C-35H	0.9296	19C-42H	0.9305	26C-50H	0.9503
5C-6C	0.9599	12C-13C	1.4413	20N-21N	1.0085	26C-51H	0.9490
5C-29H	0.9180	12C-36H	0.9302	20N-45H	0.0678	26C-52H	0.9438

Hamann approximation. Although the computational model considers the isolated molecule in the gas phase without an underlying metallic substrate, the simulated STM profiles provide a useful theoretical reference. Constant-current images at different bias voltages offer a clear spatial representation of the nucleophilic and electrophilic regions. The bright features in the simulated topographs represent regions of enhanced electron density associated with the HOMO and LUMO, highlighting the distinct electronic contrast between the rigid, electron-rich 2,6-diphenylpiperidin-1-ol core and the highly polarizable hydrazone linkage. This spatial distribution reveals the anisotropic electronic character of molecule, which may influence its optical and biological properties.

Effect of temperature on entropy (S), constant volume heat capacity (C_V) and constant-pressure heat capacity (C_P): Thermodynamic parameters, including entropy (S), isochoric heat capacity (C_V) and isobaric heat capacity (C_P), were calculated using the Shermo program [51] and the results are shown in Table-10. These parameters are temperature dependent; with increasing temperature, enhanced excitation of vibrational, rotational and translational modes increase molecular disorder and entropy. Similarly, the increasing accessibility of energy levels enhances the capacity of molecule to absorb and store thermal energy, resulting in higher heat-capacity values.

$$S = 65.3340 + 0.3322\ T - 5.0595\ e^{-5}\ T^2\ (0.9999)$$

$$C_V = -1.8184 + 0.3322\ T - 1.5232\ e^{-4}\ T^2\ (0.9992)$$

$$C_P = 0.16858 + 0.3804\ T - -1.5232\ e^{-4}\ T^2\ (0.9992)$$

TABLE-10
EFFECT OF TEMPERATURE ON
S, C_V AND C_P FOR THE TITLED MOLECULE

Temperature (K)	S (cal/mol/K)	C_V (cal/mol/K)	C_P (cal/mol/K)
100	99.147	37.511	39.498
200	129.600	65.501	67.488
300	159.257	96.059	98.046
400	189.162	126.037	128.024
500	218.662	151.905	153.892
600	247.067	173.063	175.050
700	274.042	190.281	192.268
800	299.502	204.474	206.461
900	323.493	216.351	218.338
1000	346.108	226.410	228.397

Polynomial fitting was employed to describe the temperature dependence of the thermodynamic parameters and predict their behaviour over a broad temperature range. These correlations provide insights into the thermal characteristics and energy profile of the substituted organic framework. The data show a consistent increase in entropy (S), heat capacity at constant volume (C_V) and heat capacity at constant pressure (C_P) from 100 to 1000 K. Entropy increases from 99.147 to 346.108 cal mol^{-1} K^{-1}, while C_V and C_P increase from approximately 37-39 to 226-228 cal mol^{-1} K^{-1}. This behaviour arises from the progressive population of vibrational, rotational and translational states with increasing temperature.

The temperature dependence is well described by polynomial fits, with R^2 values of 0.9999 for entropy and 0.9992 for heat capacities. The entropy follows the relation $S = 65.3340 + 0.3322T - 5.0595 \times 10^{-5}\ T^2$. These strong correlations demonstrate the reliability of the calculated thermodynamic trends over the investigated temperature range. However, the polynomial fits themselves should not be considered evidence of molecular geometry optimization or structural stability; these aspects are established independently through the geometry optimization and energy-convergence results (Fig. 1d-e).

Average local ionization energy (ALIE) analysis: Average local ionization energy (ALIE) is a useful quantum chemical descriptor for identifying regions with weakly bound electrons and potential sites for electrophilic attack [52]. Lower ALIE values correspond to regions where electron removal is energetically more favourable, providing insights into molecular reactivity. Unlike global descriptors, ALIE offers a three-dimensional representation of the spatial distribution of electron-binding strength, particularly around lone pairs and π-electron systems. For the title molecule, ALIE analysis was performed using Multiwfn 3.8 and the resulting colour-coded surface map is shown in Fig. 11 and the following observations were made:

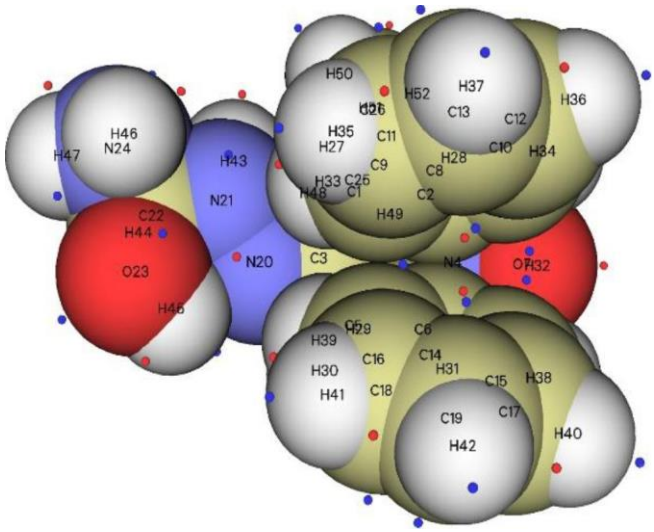

Fig. 11. ALIE for the titled molecule

Electrophilic attack sites (red/blue points): The surface exhibits distinct red and blue regions corresponding to localized variations in ionization energy. The most prominent low-ALIE regions are concentrated around the oxygen atoms O23 and O7 and the nitrogen centers N24, N21 and N20. These features are associated with the lone pairs of the heteroatoms, identifying these sites as regions of enhanced susceptibility toward electrophilic attack.

Aromatic π-system reactivity: The phenyl rings (C13, C12, C19, C17, *etc.*) exhibit a yellowish-green surface, corresponding to moderate ALIE values. This suggests that the delocalized π-electron systems may serve as secondary sites for electrophilic aromatic substitution.

Structural correlation: The ALIE map is consistent with the 3D molecular structure, showing that the highest reactivity is localized around the hydrazone linkage and hydroxyl groups, while the aromatic framework contributes to the electronic stabilization. The optimized ground-state geometry

further supports the reliability of the ALIE analysis. Together with the MEP surface, the ALIE results identify the heteroatom rich regions as dominant nucleophilic sites, which may facilitate hydrogen-bonding interactions with the 1BP1 receptor observed in the docking study.

Docking studies: The prepared 1BP1 protein and energy minimized ligand were subjected to molecular docking using PyRx. The title compound showed a docking score of -6.4 kcal mol^{-1}, with the docking details and interaction profile presented in Table-11, respectively.

TABLE-11
HYDROGEN BONDING STYLE AND BOND DISTANCE BETWEEN THE DONOR AND ACCEPTORS

Name of the atom	Name of the amino acid	Hydrogen bond distance (Å)
H	PRO A: 430	2.14
O	VAL A: 433	2.05
H	VAL A: 433	2.67
H	ASN A: 373	2.58
H	THR A: 429	2.35

The ligand occupied the binding pocket through hydrogen-bonding and close-contact interactions with key amino acid residues (Fig. 12). Five hydrogen bonds were observed in the docked complex. VAL A:433 formed two hydrogen bonds at 2.05 and 2.67 Å, while PRO A:430, THR A:429, and ASN A:373 formed interactions at 2.14, 2.35 and 2.58 Å, respectively. The short bond distances support favourable ligand–protein interactions within the binding site. The nitrogen and oxygen atoms of the piperidine–hydrazone framework participate in hydrogen bonding, while the aromatic and hydrophobic portions of the molecule occupy complementary non-polar regions of the pocket.

Molecular docking with human bactericidal/permeability increasing protein (BPI; PDB ID: 1BP1) was carried out to assess the possible biological relevance of the synthesized compound. BPI is involved in host defence against Gram-negative bacteria through its interaction with bacterial lipopolysaccharides. The docking score of -6.4 kcal mol^{-1} represents a moderate predicted binding affinity for the selected protein. This computational value should not be interpreted as direct evidence of experimental binding affinity or biological activity.

The hydrogen-bonding network involving VAL A:433, PRO A:430, THR A:429, and ASN A:373 provides a plausible basis for ligand stabilization within the 1BP1 binding pocket. The heteroatom-rich piperidine–hydrazone framework may contribute to the observed protein–ligand interactions. The molecular dynamics simulations, binding free-energy calculations and experimental biological assays would be required to establish the stability and biological significance of the predicted complex.

Conclusion

The present investigation provides a detailed quantum-chemical characterization of the hydrazone-linked piperidine derivative using DFT calculations and molecular docking analysis. The optimized structure was found to be energetically stable, while the calculated HOMO–LUMO energy gap of 5.6665 eV suggests relatively high kinetic stability and low chemical reactivity. NBO and NCI analyses further support the stabilization of the molecular framework through significant hyperconjugative interactions and intermolecular/intramolecular noncovalent interactions, particularly hydrogen bonding. The calculated nonlinear optical (NLO) parameters reveal a hyperpolarizability approximately three times higher than that of urea, suggesting potential for further investigation in photonic and optoelectronic applications. Molecular docking against the 1BP1 protein yielded a binding affinity of -6.4 kcal/mol, indicating a favourable interaction between the compound and the target binding site. These computational findings support further experimental investigation of the compound including its synthesis, physico-chemical characterization and biological evaluation.

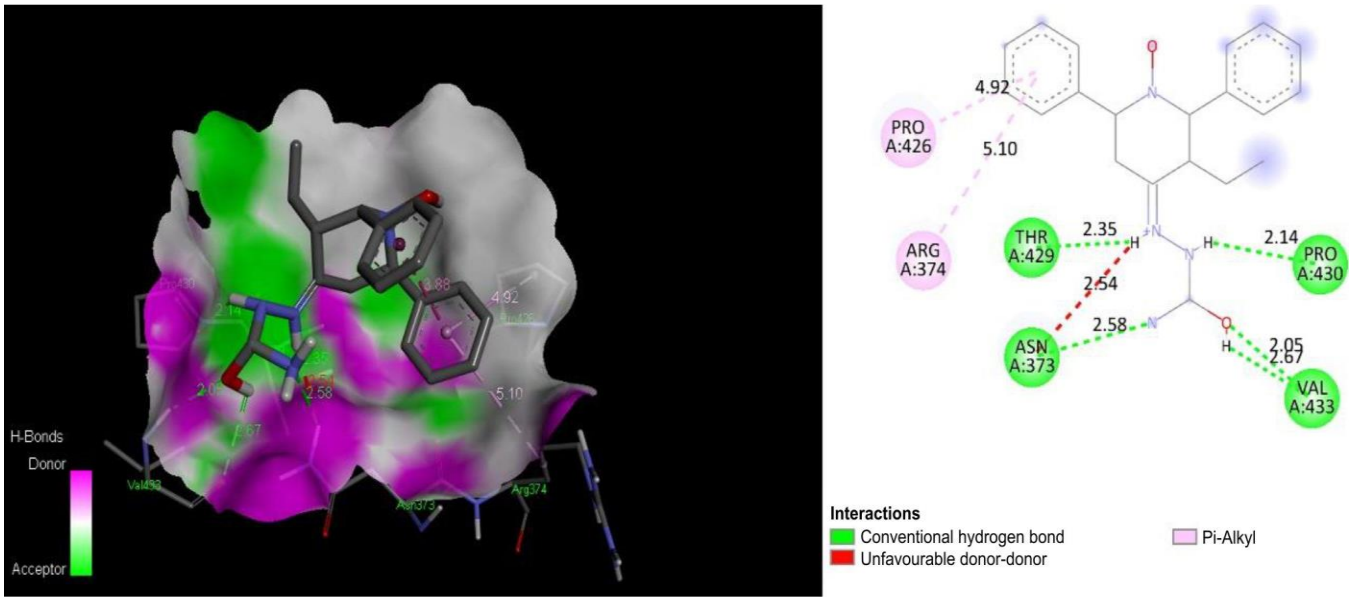

Fig. 12. Docking pattern between the titled molecule and the protein 1BP1

ACKNOWLEDGEMENTS

The authors are thankful to the Principal, the Secretary and the Management of St. John's College, Palayamkottai for providing the computer and software facilities.

CONFLICT OF INTEREST

The authors declare that there is no conflict of interests regarding the publication of this article.

DECLARATION OF AI-ASSISTED TECHNOLOGIES

During the preparation of this manuscript, the authors used an AI-assisted tool(s) to improve the language and no data, results or scientific conclusions were generated by AI. All analyses, interpretations and conclusions are the authors' own. The authors reviewed and edited the content and take full responsibility for the published work.

REFERENCES

1. I.A. Mir, Q.U. Ain, T. Qadir, A.Q. Malik, S. Jan, S. Shahverdi and S.A. Nabi, *J. Mol. Struct.*, **1295**, 136216 (2024); https://doi.org/10.1016/j.molstruc.2023.136216
2. G. Korkmaz, *J. New Results Sci.*, **13**, 61 (2024); https://doi.org/10.54187/jnrs.1464723
3. I. Pal, S. Dutta, F. Basuli, S. Goverdhan, S.-M. Peng, G.-H. Lee, and S. Bhattacharya, *Inorg. Chem.*, **42**, 4338 (2003); https://doi.org/10.1021/ic034247j
4. P. Sharma, A. Kumar and M. Sharma, *Indian J. Chem.*, **45A**, 872 (2006).
5. A.A. Aly, E.M. Abdallah, S.A. Ahmed, M.M. Rabee and S. Bräse, *Molecules*, **28**, 1808 (2023); https://doi.org/10.3390/molecules28041808
6. J.B. Veeramalini, V. Narayanan and G. Baskar, *J. Chem. Pharm. Res.*, **7**, 228 (2015).
7. D.B. Reddy, A.S. Reddy and V. Padmavathi, *J. Chem. Res. (S)*, **12**, 784 (1998); https://doi.org/10.1039/a804381g
8. M. Palaniappa, M. Jayalakshmi, B.R.V. Narasimhan and K. Balasubramanian, *Int. J. Electrochem. Sci.*, **3**, 656 (2008); https://doi.org/10.1016/S1452-3981(23)15551-9
9. M. Palaniappa, M. Jayalakshmi, P.M. Prasad and K. Balasubramanian, *Int. J. Electrochem. Sci.*, **3**, 452 (2008); https://doi.org/10.1016/S1452-3981(23)15465-4
10. L. Fotouhi, N. Farzinnegad, M.M. Heravi and Sh. Khaleghi, *Bull. Korean Chem. Soc.*, **24**, 1751 (2003); https://doi.org/10.5012/bkcs.2003.24.12.1751
11. M. Noel and K.I. Vasu, Cyclic Voltammetry and the Frontiers of Electrochemistry, Oxford and IBH Publishing Co. Pvt. Ltd., New Delhi (1990).
12. D.W. Shoesmith, S. Sunder, M.G. Bailey, G.J. Wallace and F.W. Stanchell, *J. Electroanal. Chem. Interfacial Electrochem.*, **143**, 153 (1983); https://doi.org/10.1016/S0022-0728(83)80261-7
13. P. Sharma, A. Kumar and M. Sharma, *Indian J. Chem.*, **43B**, 2431 (2004).
14. P. Sharma, A. Kumar, M. Sharma and S. Upadhyay, *Indian J. Chem.*, **43B**, 2653 (2004).
15. J. Amalraj, C.E. Vergara, M. Monroy-Cárdenas, R. Araya-Maturana and M. Martínez-Cifuentes, *Int. J. Mol. Sci*., **23**, 15043 (2022); https://doi.org/10.3390/ijms232315043
16. S.A.M. Refaey, A.A. Hassan and H.S. Shehata, *Int. J. Electrochem. Sci.*, **3**, 325 (2008); https://doi.org/10.1016/S1452-3981(23)15457-5
17. R. Sangtyani, V. Kumar, P.S. Verma, A.K. Varshney and S. Varshney, *J. Indian Chem. Soc.*, **88**, 1553 (2011).
18. S.G. Kini, R. Rajappan, V.P. Ramachandran, A. Govindakarnavar, K.S.R. Pai and S. Dharmarajan, *Drug Des. Dev. Ther.*, **9**, 3779 (2015); https://doi.org/10.2147/DDDT.S83047
19. P. Sumathi, K. Kiruthiga, R. Sivaraj, P. Mosae Selvakumar and I.V.M.V. Enoch, *Anal. Bioanal. Chem. Res.*, **9**, 235 (2022); https://doi.org/10.22036/abcr.2021.182833.1337
20. N. Mardirossian and M. Head-Gordon, *Mol. Phys.*, **115**, 2315 (2017); https://doi.org/10.1080/00268976.2017.1333644
21. T. Van Mourik, M. Bühl and M. Gaigeot, *Philos. Trans. A Math. Phys. Eng. Sci.*, **372**, 20120488 (2014); https://doi.org/10.1098/rsta.2012.0488
22. ACD/ChemSketch, version 1.2, Advanced Chemistry Development, Inc. (ACD/Labs), Toronto, Canada (2020).
23. M.D. Hanwell, D.E. Curtis, D.C. Lonie, T. Vandermeersch, E. Zurek and G.R. Hutchison, *J. Cheminform.*, **4**, 17 (2012); https://doi.org/10.1186/1758-2946-4-17
24. M.J. Frisch, G.W. Trucks, H.B. Schlegel, G.E. Scuseria, M.A. Robb, J.R. Cheeseman, G. Scalmani, V. Barone, G.A. Petersson, H. Nakatsuji, M. Caricato, A.V. Marenich, J. Bloino, B.G. Janesko, R. Gomperts, B. X. Li, Mennucci, H.P. Hratchian, J.V. Ortiz, A.F. Izmaylov, J.L. Sonnenberg, D. Williams-Young, F. Ding, F. Lipparini, F. Egidi, J. Goings, B. Peng, A. Petrone, T. Henderson, D. Ranasinghe, V.G. Zakrzewski, J. Gao, N. Rega, G. Zheng, W. Liang, M. Hada, M. Ehara, K. Toyota, R. Fukuda, J. Hasegawa, M. Ishida, T. Nakajima, Y. Honda, O. Kitao, H. Nakai, T. Vreven, K. Throssell, J.A. Montgomery Jr., J.E. Peralta, F. Ogliaro, M.J. Bearpark, J.J. Heyd, E.N. Brothers, K.N. Kudin, V.N. Staroverov, T.A. Keith, R. Kobayashi, J. Normand, K. Raghavachari, A.P. Rendell, J.C. Burant, S.S. Iyengar, J. Tomasi, M. Cossi, J.M. Millam, M. Klene, C. Adamo, R. Cammi, J.W. Ochterski, R.L. Martin, K. Morokuma, O. Farkas, J.B. Foresman and D.J. Fox, Gaussian 16, Revision B.01, Gaussian, Inc., Wallingford, CT (2016).
25. A.D. Becke, *J. Chem. Phys.*, **98**, 5648 (1993); https://doi.org/10.1063/1.464913
26. C. Lee, W.X. Yang and R.G. Par, *Phys. Rev. B Condens. Matter*, **37**, 785 (1988); https://doi.org/10.1103/PhysRevB.37.785
27. N.M. O'boyle, A.L. Tenderholt and K.M. Langner, *J. Comput. Chem.*, **29**, 839 (2008); https://doi.org/10.1002/jcc.20823
28. T. Lu and F. Chen, *J. Comput. Chem.*, **33**, 580 (2012); https://doi.org/10.1002/jcc.22885
29. W. Humphrey, A. Dalke and K. Schulten, *J. Mol. Graph.*, **14**, 33 (1996); https://doi.org/10.1016/0263-7855(96)00018-5
30. S. Dallakyan and A.J. Olson, *Methods Mol. Biol.*, **1263**, 243 (2015); https://doi.org/10.1007/978-1-4939-2269-7_19
31. BIOVIA, Dassault Systèmes, Discovery Studio Visualizer, V21.1.0. 20298, San Diego: Dassault Systèmes (2021).
32. S. Armaković, S. Armaković, S.J. Armaković and S.J. Armaković, *Computation*, **13**, 216 (2025); https://doi.org/10.3390/computation13090216
33. S. Armaković, S. Armaković, S.J. Armaković and S.J. Armaković, *Mol. Simul.*, **50**, 560 (2024); https://doi.org/10.1080/08927022.2024.2329736
34. S. Armaković, S. Armaković, S.J. Armaković and S.J. Armaković, *Mol. Simul.*, **49**, 117 (2023); https://doi.org/10.1080/08927022.2022.2126865
35. G. Ramachandran, C. Ramakrishnan and V. Sasisekharan, *J. Mol. Biol.*, **7**, 95 (1963); https://doi.org/10.1016/S0022-2836(63)80023-6
36. V.A. Adole, I. Danish, J. Kores, J. Jebaraj, S. Janani, S.K. Ghotekar and R.D. Amrutkar, *Results Chem.*, **13**, 101951 (2025); https://doi.org/10.1016/j.rechem.2024.101951
37. J.J. Kores, I.A. Danish, T. Sasitha, J.G. Stuart, E.J. Pushpam and J.W. Jebaraj, *Heliyon*, **7**, e08377 (2021); https://doi.org/10.1016/j.heliyon.2021.e08377
38. R.G. Parr and W. Yang, *J. Am. Chem. Soc.*, **106**, 4049 (1984); https://doi.org/10.1021/ja00326a036
39. K. Fukui, *Science*, **218**, 747 (1982); https://doi.org/10.1126/science.218.4574.747
40. A.P. Bandyopadhyay, A. Karmakar, J. Deb, U. Sarkar and M.M. Seikh, *Spectrochim. Acta A Mol. Biomol. Spectrosc.*, **228**, 117827 (2020); https://doi.org/10.1016/j.saa.2019.117827
41. J. Poater, M. Duran, M. Solà and B. Silvi, *Chem. Rev.*, **105**, 3911 (2005); https://doi.org/10.1021/cr030085x
42. C. Bird, *Tetrahedron*, **41**, 1409 (1985); https://doi.org/10.1016/S0040-4020(01)96543-3

43. E. Matito, M. Duran and M. Solà, *J. Chem. Phys.*, **122**, 014109 (2005); https://doi.org/10.1063/1.1824895
44. T.M. Krygowski, *J. Chem. Inf. Comput. Sci.*, **33**, 70 (1993); https://doi.org/10.1021/ci00011a011
45. H.L. Schmider and A.D. Becke, *J. Mol. Struct. THEOCHEM*, **527**, 51 (2000); https://doi.org/10.1016/S0166-1280(00)00477-2
46. T. Lu and F. Chen, *J. Phys. Chem. A*, **117**, 3100 (2013); https://doi.org/10.1021/jp4010345
47. I. Mayer, *Chem. Phys. Lett.*, **97**, 270 (1983); https://doi.org/10.1016/0009-2614(83)80005-0
48. J. Tersoff and D.R. Hamann, *Phys. Rev. B Condens. Matter*, **31**, 805 (1985); https://doi.org/10.1103/PhysRevB.31.805
49. C.J. Chen, Introduction to Scanning Tunneling Microscopy, Oxford University Press, Oxford, edn. 2 (2008).
50. T. Lu and Q. Chen, *ChemRxiv* (2020); https://doi.org/10.26434/chemrxiv.12278801.v1
51. P. Sjoberg, J.S. Murray, T. Brinck and P. Politzer, *Can. J. Chem.*, **68**, 1440 (1990); https://doi.org/10.1139/v90-220